Microwave sea ice and ocean brightness temperature and emissivity between 22 and 243 GHz from ship-based radiometers

Janna E. RÜCKERT[1], Andreas WALBRÖL[2], Nils RISSE[2], Pavel KROBOT[2], Rainer HASENEDER-LIND[2], Mario MECH[2], Kerstin EBELL[2], and Gunnar SPREEN[1]

[1]*Institute of Environmental Physics, University of Bremen, Bremen, Germany*

[2]*Institute for Geophysics and Meteorology, University of Cologne, Cologne, Germany*

Correspondence: Janna E. Rückert <janna.rueckert@uni-bremen.de>

ABSTRACT. Passive microwave measurements of Arctic sea ice have been conducted over the last 50 years from space and during airborne, ship-, and ground-based measurement campaigns. The different radiometric signatures of distinct surface types have led to satellite retrievals of, e. g., sea ice concentration. In contrast, ground-based upward-viewing radiometers measure radiation emitted from the atmosphere and are used to retrieve atmospheric variables. Here, we present results from a ship-based radiometer setup with a mirror construction, which allows us to switch between atmospheric and surface measurements flexibly. This way, in summer 2022, surface observations in the Arctic marginal sea ice zone could be performed from the research vessel *Polarstern* by two radiometers covering the frequency range from 22 to 243 GHz. At low frequencies, the brightness temperatures show clear signatures of different surface conditions. We estimate emissivities at 53◦ zenith angle from infrared-based skin temperatures. Predominantly vertically-polarized 22 to 31 GHz emissivities are between 0.51 and 0.55 for open ocean and around 0.95 for sea ice. Pedominantly horizontally-polarized 243 GHz ocean emissivities are around 0.78 and ice surfaces exhibit a large variability from 0.67 to 0.82. Our results can improve the characterization of surface emissions in satellite retrieval algorithms.

INTRODUCTION

Changes in global climate are most prominent in the Arctic where the near-surface temperature increase in the last decades is about four times higher than the global mean (Rantanen and others, 2022), a phenomenon that is called Arctic amplification (Wendisch and others, 2023). To comprehend these amplified changes and feedback mechanisms, we need observations of crucial climate variables such as sea ice concentration, liquid water path (LWP), and integrated water vapor (IWV). However, these observations are sparse and challenging to obtain. For upward-viewing microwave radiometers (MWRs), retrievals algorithms for IWV and LWP are well established (Westwater, 1978; Ebell and others, 2017) and the observations can be used to monitor these atmospheric parameters, but suffer from spatial coverage especially in higher latitudes. Good spatial coverage of observations for IWV and LWP can in principle be achieved by polar-orbiting satellites (Crewell and others, 2021). However, deriving IWV and LWP from satellite measurements in the Arctic is challenging because of the often high and highly variable emissivity of the (snow-covered) sea ice. The surface contribution to the overall signal needs to be known for an accurate retrieval of atmospheric parameters from downward-viewing instruments. Although, over the last fifty years, passive microwave measurements of Arctic sea ice have been conducted from a variety of platforms, including aircraft, ships, and on-ice stations (e.g., Wilheit and others, 1971; Gloersen and others, 1973; Mätzler and others, 1984; Hollinger and others, 1984; Grenfell and Lohanick, 1985), they are still rare in the marginal sea ice zone and more measurements are required.

Here, we present an instrumentation setup allowing for atmospheric and surface measurements. Two mirrors fixed to the stand of two MWRs operated on the research vessel *Polarstern* in summer 2022, enabled alternating surface and atmosphere observations. The measurements were performed in the marginal sea ice zone during the cruise ATlantic WAter pathways to the ICE in the Nansen Basin and Fram Strait (ATWAICE) (Kanzow, 2023). The mirror construction allowed us to observe the surface hourly at different zenith angles. Measurements during ATWAICE provided the possibility to measure emissivities in varying ocean and ice conditions in a wide frequency range from 22 to 243 GHz, including measurements of horizontal variability during transects. This is particularly important for satellite retrievals as satellite footprints are of the order of kilometers.

In this manuscript, we first describe the calculation of surface emissivities and the principal instrumentation setup. We then show results from the surface brightness temperature (TB) measurements. We finally estimate surface emissivities using additional surface observations by thermal infrared imagery and

estimations of downwelling atmospheric radiation.

CALCULATION OF SURFACE EMISSIVITIES

When observing a surface target with a radiometer close to the surface, the brightness temperature T_b is related to the physical target temperature T and an emission coefficient ϵ (hereafter called emissivity) via (Mätzler and others, 1984)

$$T_b = \epsilon T + (1 - \epsilon)T_{b,atm}, \tag{1}$$

where $T_{b,atm}$ is the downwelling radiation emitted by the atmosphere. In principle, ϵ is a function of frequency and is determined by the dielectric properties of the surface material and the interface properties, e. g., roughness, between the surface and the atmosphere. Because the microwave radiation can be emitted from within the snow-ice-water system, vertical gradients of the temperature and the microstructure influence T_b. In our case, we assume an isothermal target. This is a reasonable assumption during summer which is supported by the low temperature gradients measured during the ice stations (see next section). Therefore, we use the surface temperature T_s as T here. Thus, ϵ is given by

$$\epsilon = \frac{(T_b - T_{b,atm})}{(T_s - T_{b,atm})}, \tag{2}$$

where the additional quantities $T_{b,atm}$ and the surface temperature T_s are required and must be estimated by auxiliary observations. For Eq. 2 to be valid, the interaction of the radiation with the atmosphere between the radiometer (here at a height of 22 m above sea level) and the target (i. e., the surface) must be negligible.

CAMPAIGN AND MEASUREMENT SETUP

Expedition PS131 ATWAICE

The expedition PS131 of *Polarstern* named ATWAICE (Kanzow, 2023) took place from 28 June to 17 August 2022, both starting and ending in Bremerhaven (Fig. 1). The multidisciplinary study of the marginal ice zone began on 11 July 2022. The measurement program included several transects from the ice-free ocean across the marginal ice zone into the pack ice. In the pack ice, three ice floe stations with atmosphere, ice, and ocean measurements were established and revisited one week after their first visits.
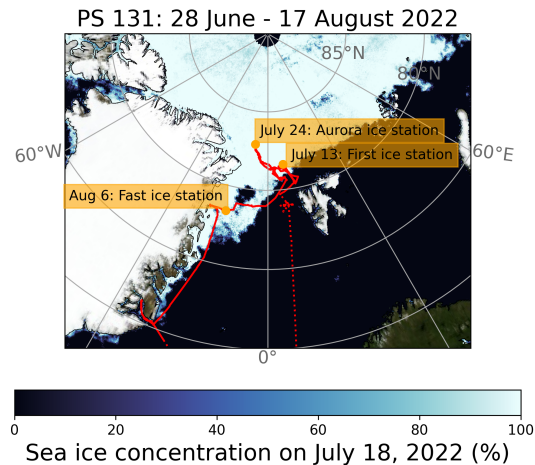
PS 131: 28 June - 17 August 2022

Sea ice concentration on July 18, 2022 (%)

Fig. 1. *Polarstern* track (red line) during ATWAICE. Shown in the background is the sea ice concentration product on 18 July 2022, operationally available at www.seaice.uni-bremen.de (ASI algorithm; Spreen and others, 2008).

From 23 to 26 July, *Polarstern* passed through compact ice to the Aurora vent field around $82\circ58'$N with higher ice thicknesses. Afterward, the three ice station floes were each revisited for the third and final time. On 3 August, *Polarstern* headed toward East Greenland and entered fast ice (less than $1\,$m ice thickness). On 7 August, *Polarstern* moved south and reached Scoresby Sund, Greenland, near $70\circ$N on 9 August. We ended our MWR measurements on 12 August.

Various sea ice and atmospheric conditions were sampled during the cruise (Fig. 2). The sea ice concentration varies mostly from 60 to 100% as derived from visual observations within one nautical mile from *Polarstern* following the Ice Watch observation protocol (Hutchings and others, 2020) between 11 July and 9 August available at `https://icewatch.met.no/`. These values might not be representative for the sea ice concentration near the ship viewed by the radiometers. Open melt ponds were observed all the time, with the highest area fractions above 50% on the fast ice. The median air temperatures measured on board *Polarstern* at about $29\,$m above sea level from 11 July to 21 August is $0.4\circ C$ with a minimum of $-1.7\circ C$ (4 August) and maximum of $10.7\circ C$ (18 July) when moist and warm air reached the Fram Strait.

Instrumentation

The measurements described here were conducted as part of the WAter vapor, cloud Liquid water, and Surface Emissivity over the Arctic marginal ice zone in summer (WALSEMA) project embedded within the Transregional Collaborative Research Centre TRR-172 'ArctiC Amplification: Climate Relevant Atmospheric and SurfaCe Processes, and Feedback Mechanisms (AC)[3]' (Wendisch and others, 2023).
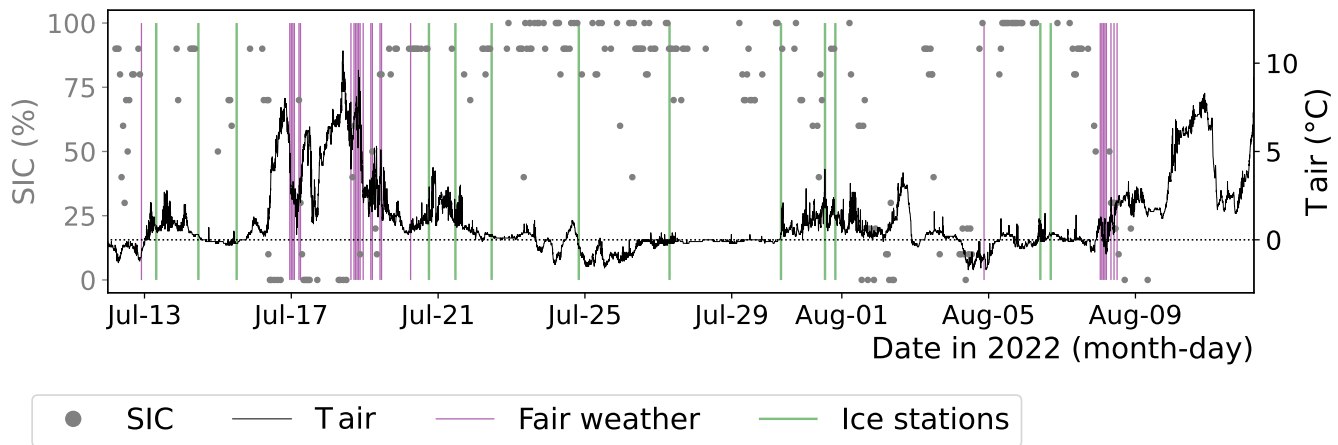
Fig. 2. Time series of sea ice concentration (SIC), air temperature (T air, secondary axis), fair weather intervals, and occurrence of ice stations from 12 July to 12 August 2022. The sea ice concentration is estimated in steps of 10% until 9 August 2022.

Microwave radiometers

The two microwave radiometers Humidity And Temperature PROfiler (HATPRO; Rose and others, 2005) and Microwave Radar/radiometer for Arctic Clouds - Passive (MiRAC-P; Mech and others, 2019) were installed on *Polarstern's* top deck ('Peildeck') on starboard (see Fig. 3). HATPRO measures TBs at seven channels between 22 and 31 GHz with the 22.24 GHz channel being close to the water absorption line (receiver 1), and at seven channels in the 58 GHz oxygen absorption complex (receiver 2). MiRAC-P utilizes six channels along the 183 GHz water vapor line (receiver 1) and two window channels at 243 and 340 GHz (receiver 2). Unfortunately, the receiver at 340 GHz failed at the beginning of the cruise. Both MWRs measure with 1 s integration time. Internally, both radiometers contain a rotatable mirror that can change the incidence angle, and a wire grid that separates the incoming radiation in vertically and horizontally-polarized fractions, so that at each frequency, one of these fractions is measured by the receivers (more about the polarization below). The instruments' specifications are listed in Table 1. An absolute calibration with liquid nitrogen was performed twice during the cruise (7 and 30 July 2022). We estimate the uncertainty in TBs because of these calibrations to be below 1 K. The radiometers pointed zenith for 45 minutes per hour to derive temperature and humidity profiles, IWV, and LWP, and toward the mirrors for about 15 minutes per hour. For the data analysis we used only data where the flag *visual_inspection_filter*, indicating reduced data quality (e. g., because of a wet radom, provided with the data), was not set.

Mirrors and polarization

Fixed to the stands of the MWRs, aluminum plates with a size of $0.55\,\mathrm{m}^2$ were installed as external rotatable mirrors (see Fig. 4). This mirror setup was developed for this cruise and deployed for the first time. It redirects upwelling radiation from $53\,\circ$ zenith angle, i.e., the typical angle of operational satellite microwave imagers, to the MWR receivers. As we are not observing in zenith direction, this corresponds to an uneven distribution of the polarized radiation to the receivers, resulting in polarization mixing of the linear polarized contributions. The plane of incidence defining vertical and horizontal polarization is the plane containing the direction of the upwelling radiation from the surface from $53\,\circ$ zenith angle and the surface normal to the Earth's surface. Then the contribution of vertically-polarized TB, $T_{\mathrm{b,v}}$, and of horizontally-polarized TB, $T_{\mathrm{b,h}}$, to the overall mixed polarization signal is given by

$$T_{\mathrm{b,1}} = T_{\mathrm{b,h}} \cos(53\,\circ)^2 + T_{\mathrm{b,v}} \sin(53\,\circ)^2 \tag{3}$$
$$\approx 0.36 \cdot T_{\mathrm{b,h}} + 0.64 \cdot T_{\mathrm{b,v}}$$

for receiver 1 (between 22 and 31 GHz and along the 183 GHz line) and

$$T_{\mathrm{b,2}} = T_{\mathrm{b,h}} \sin(53\,\circ)^2 + T_{\mathrm{b,v}} \cos(53\,\circ)^2 \tag{4}$$
$$\approx 0.64 \cdot T_{\mathrm{b,h}} + 0.36 \cdot T_{\mathrm{b,v}}$$

for receiver 2 (58 GHz oxygen absorption complex, at 243 and at 340 GHz; equations following personal communication with manufacturer RPG). We thus call the polarization of $T_{\mathrm{b,1}}$, according to the dominating polarization, predominantly-vertical (PV), which corresponds to the channels between 22 and 31 GHz and along the 183 GHz water vapor line. And for $T_{\mathrm{b,2}}$ we call the polarization predominantly-horizontal (PH), which corresponds to all other frequency channels. We assume that the mirrors are perfectly reflective. Ship motions resulted in a few degree deviations from this target zenith angle. We routinely manually dried the mirror surface in foggy conditions due to the lack of preventive measures like heating. However, the presence of liquid droplets creates potential uncertainty. The mirror was rotated manually five times during the cruise to scan various zenith angles. However, these scans are inconclusive due to heterogeneous ice surfaces, such as melt ponds and leads, and not presented here.

Table 1. The HATPRO and MiRAC-P frequency, polarization for our setup (assuming 53 ∘ zenith angle, either predominantly vertical (PV) or predominantly horizontal (PH), half power beam width, and footprint geometry. The footprint geometry is calculated for 53 ∘ zenith angle, 22 m instrument height, and without ship motion.

Instrument	Frequency (GHz)	Polarization	Beam width (∘)	Footprint (m^2)
HATPRO	22.24, 23.04, 23.84, 25.44, 26.24, 27.84, 31.4	PV	3.7–3.3	4.0×2.4–3.6×2.2
HATPRO	51.26, 52.28, 53.86, 54.94, 56.66, 57.3, 58.0	PH	2.5–2.2	2.7×1.6–2.4×1.4
MiRAC-P	183.31±0.6, ±1.5, ±2.5, ±3.5, ±5.0, ±7.5	PV	1.3	1.4×0.8
MiRAC-P	243	PH	1.25	1.4×0.8
MiRAC-P	340[a]	PH	1.1	1.1×0.7

[a]the 340 GHz receiver was malfunctioning.

Auxiliary measurements

A visual (VIS; GoPro HERO 10) and an infrared (IR) camera (InfraTec VarioCAM HD, 7.5 tA visual (VIS; GoPro HERO 10) and an infrared (IR) camera (InfraTec VarioCAM HD, 7.5 to 14 μm) observing the surface as well as a sky camera (VIS and IR) were complementing the microwave measurements and provide context for the interpretation of the data. The surface-facing cameras were installed next to the radiometers on the deck (see Fig. 3) and took images every 5 s. An inertial motion unit (IMU) measuring roll and pitch angles was installed on top of the IR camera. The resulting angles measured with the IMU were used to project the IR data to the ground. Missing IMU data due to instrument or recording issues were filled using the average angle of the respective day.

Additionally, on-ice measurements of the ice and surface conditions conducted during twelve ice stations are available. Here, ice cores were taken to measure vertical profiles of density, temperature, and salinity in the sea ice (Rückert and others, 2023a,b). During the time of the campaign, the snow on the sea ice had already melted. The resulting surface scattering layer was described using traditional snow pit methods. The microwave radiometer footprint was sampled on 24 July, 31 July, and 6 August. Results of most of the measurements are given in the cruise report (Kanzow, 2023). In summary, the spatial variability of some of the surface and ice parameters, e.g., the diameters of the crystals making up the uppermost layer or the ice thickness in some cases, was high and could change significantly within a few meters.
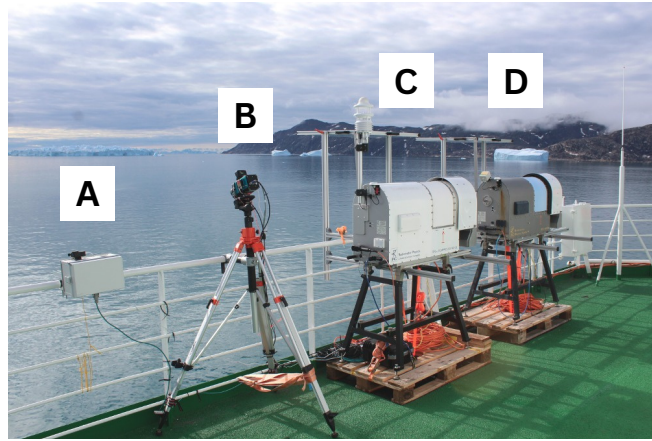
Fig. 3. (A) Sky camera, (B) IR surface camera with VIS surface camera on top, (C) MiRAC-P, and (D) HATPRO on board *Polarstern*.
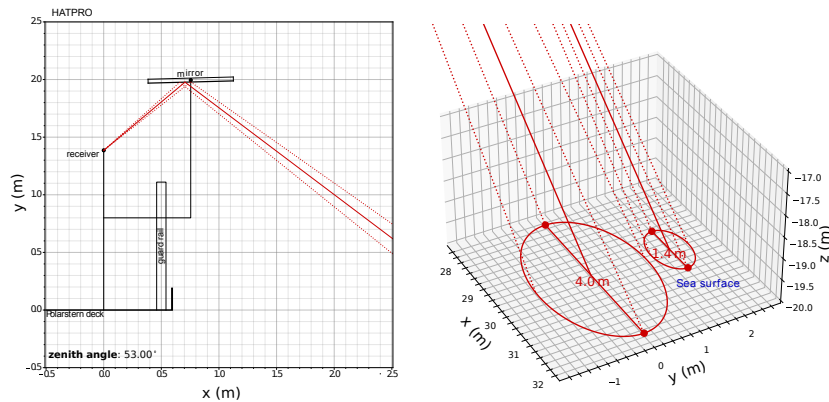

Fig. 4. Mirror setup. Left: The receiver of the radiometer is positioned at x=0 m with an elevation angle of 40∘. Because of the mirror alignment, this results in a zenith angle of 53∘. The mirror has a size of $0.55\,\mathrm{m}^2$. The red lines are the path of rays of the microwave radiation with the center and the outer rays obtained from the beam width (3dB). Right: projected footprints of HATPRO (left ellipse) and MiRAC-P (right ellipse) on the surface.

RESULTS AND DISCUSSION

Surface observations: brightness temperatures

Before looking at the overall statistics of the measured surface TBs during the ship cruise, we first focus on two case studies, which help to introduce and interpret the MWR observations. These two cases of MWR surface observations under different atmospheric and sea ice conditions on 18 July and 8 August 2022, are shown in Figs. 5 and 6, respectively. Small gaps in the time series correspond to internal instrument calibrations. In addition, IR and VIS imagery at three times are also shown and calculated MWR footprints are marked by ellipses in the IR imagery. These ellipses might be slightly misplaced because of uncertainties in the timestamp and slightly changing zenith angles due to ship motion. However, we still expect them to be within the black rectangle shown in the IR imagery. In the following, we refer to the observations in the different channels using the observed frequencies, which always implies a specific channel-dependent polarization (listed in Table 1).

Case 1: 18 July 2022

On 18 July 2022 (Fig. 5), *Polarstern* was moving slowly with a mean speed of 0.25 ms and we can see small ice floes drifting in and out of the footprint. The distance from the start (at 80∘49.48′N, 9∘9.96′E) to the endpoint of the measurements is about 0.2 km. The sea ice temperatures are around 0 ∘C and ocean temperatures are slightly colder. On this day, a warm air intrusion occurred in the measurement area and air temperatures were well above freezing with an average of 7.0 ∘C during the surface observation. The atmospheric HATPRO measurements right before and after the surface observation yield IWV values of 16.4 and $16.1 \, \mathrm{kg \, m^{-2}}$, respectively.

Fig. 5a and b show the HATPRO TBs at 22 to 31 GHz and at frequencies in the 58 GHz oxygen absorption complex, respectively. TBs at 22 to 31 GHz show lower values (about 160 K) over open ocean than over sea ice (about 250 K). In addition to the surface-driven variability of the TBs resulting in TB changes of up to 90 K, small periodic oscillations of the order of a few Kelvin are visible at these frequencies.

At 51.26 and 52.28 GHz, TBs over open ocean are about 220 and 240 K, respectively, and about 265 K over sea ice. Qualitatively, their behavior is similar to the 22 to 31 GHz range. At frequencies between 54.94 to 58 GHz, an opposite behavior can be seen with slightly higher (about 3 K) TBs over the ocean than over the sea ice, with TBs ranging between 273 to 278 K. No changes with changing surface conditions

are observed at 53.86 GHz, showing almost constant TBs of about 273 K (with a standard deviation below 1 K).

Fig. 5c and d show the TBs measured by the MiRAC-P radiometer at frequencies in the 183 GHz water vapor line and at 243 GHz, respectively. Due to instrument settings, the measurement period ended about 2 minutes earlier than the HATPRO measurements. TBs in the 183 GHz water vapor line change little (about 1 K) during the observation period and are around 277 K. At the 243 GHz window channel, TBs show lower values (about 264 K) over open ocean than over sea ice (about 269 K).

We can conclude that we find a clear surface signal from ice and ocean in the TBs of the frequencies for which the atmosphere is rather transparent, i.e., where $T_{\mathrm{b,atm}}$ in Eq. 1 is low (in this case 22 to 31 GHz, 51.26 and 52.28 GHz). Lower TBs occur over the highly reflective ocean compared to the highly emissive ice for the TBs between 22 to 31 GHz and TBs at 51.26 and 52.28 GHz. The small-scale oscillations correspond to changing zenith angles due to periodic ship motions. However, at frequencies in the oxygen absorption complex where the atmosphere is rather opaque (54.94 to 58 GHz), an opposite behavior can be seen with higher TBs over the ocean and lower TBs over the sea ice. For these frequencies, the reflected atmospheric signal $T_{\mathrm{b,atm}}$ originates only from the lowest few kilometers of the atmosphere. Due to the warm air intrusion, the lower atmosphere was very warm on this day. Therefore, a distinct reflected atmospheric signal can be found for the TBs over the ocean, which is more reflective than the sea ice.

We observe no apparent changes in TB with changing surface conditions at frequencies in the 183 GHz water vapor line. Here, the surface and atmospheric contributions cannot easily be disentangled. The atmospheric water vapor content is high enough to cause atmospheric downwelling TB of the same order as the surface temperatures. Therefore, the measured TBs are insensitive to changes in emissivity of different surface types (see Eq. 1).

At the 243 GHz window channel, the surface signal is again identified: here, the contribution by $T_{\mathrm{b,atm}}$ is lower than at frequencies along the 183 GHz water vapor line and thus differences in ice and ocean emissivities can be detected. We find higher TBs (by about 5 K) over ice than over open ocean. Still, atmospheric emissions are an order of magnitude larger than at 22 to 31 GHz and thus significantly decreases the sensitivity to surface emissivity changes. We attribute the dip seen around 17:20 UTC in the TBs at 243 GHz to a fraction of open ocean within the footprint. Because HATPRO has a larger footprint, the signal of open ocean within the footprint is less pronounced here. Since the footprints do not overlap, the decrease in TBs is not observed simultaneously.

Case 2: 8 August 2022

During the second case on 8 August 2022, *Polarstern* travelled through an area with small ice floes (around 76○14.11′ N and 15○37.36′ W; Fig. 6), covering a distance of about 3.3 km with a mean speed of 3.4 ms. Ice and ocean surfaces had similar temperatures (below 0 ○C). On that day, the general ice conditions are different from the first case as we can also observe the formation of new ice, e. g., around 5:43 UTC, which is slightly visible in the VIS and IR images. Air temperatures were close to but below 0 ○C. Atmospheric HATPRO measurements right before and after yield IWV values of 10.7 to 10.9 kg m^{-2}.

The TBs at the frequencies between 22 and 31 GHz (Fig. 6a) and at 51.26 to 52.28 GHz (Fig. 6b) change more rapidly than in the first case. Due to the faster speed of the vessel on that day, surface conditions also changed more rapidly. Here, the TBs show a qualitatively similar behavior compared to the case on 18 July with high TBs over sea ice (for example 240 to 260 K for frequencies between 22 and 31 GHz, and 240 and 250 K for 51.26 and 52.28 GHz around 5:37:20 UTC) and lower TBs over open ocean (around 155 K for frequencies between 22 and 31 GHz, and 220 and 235 K for 51.26 and 52.28 GHz). Around 5:42 UTC over new ice, TB values higher than over open ocean are detected. At frequencies between 53.86 to 58 GHz, no distinct changes with changing surface conditions are observed with slightly lower TBs at 53.86 GHz of 270 K and TBs ranging between 271 to 275 K for the other frequencies that vary little during the time period (standard deviations below 1 K).

The TBs at the four lower frequencies of the 183 GHz water vapor line (Fig. 6c) are around 271 K and also vary little during the observation period (standard deviations below 0.5 K). However, the TBs at 190.81 GHz (and to some extent also at 188.31 GHz) do vary with changing surface types. Here, we observe the opposite of what has been seen in the 22 and 31 GHz channels: lower TB values over ice at 190.81 GHz (for example 261 K at 5:37:20 UTC, indicated by B in Fig. 6) compared to the TBs over ocean (around 267 K). At the 243 GHz window channel, the same behavior can be found as well: TBs over ice (246 K at 5:37:20 UTC) are about 10 K lower than over ocean (around 256 K). Interestingly, the young ice, which was observed at several times, one example indicated by C in Fig. 6, shows another signature, where the TBs at 243 GHz are up to 263 K and thus higher than the ones observed over ocean. Such higher TBs can also be observed at earlier times during the observation period, when the VIS imagery also suggests that new ice could have been present.

Again, we conclude that distinct surface signals can be observed in the TBs of the frequencies between 22 to 31 GHz and 51.26 to 52.28 GHz. Here, also different TB signatures of ice and ocean surfaces are seen

at 190.81 GHz (and to a certain extent at 188.31 GHz) because of the lower atmospheric moisture content on 9 August compared to 18 July. The influence of the surface is also clearly visible at 243 GHz. TBs at 243 GHz are lower over ice than over ocean, except for the young ice, where they are higher, suggesting differences in emissivity between different ice types.

In the two cases, we observe higher *and* lower TBs over ice than over ocean at 243 GHz. But we also encountered cases when the TBs were the same: In Fig. 12 (in the Appendix) ice and ocean are not distinguishable at all at 243 GHz. Here, ocean and ice have similar physical temperatures (Fig. 12f). We assume that for this case, the emissivities of ice and ocean are alike at 243 GHz, which could explain why there is no signal in TB at 243 GHz of the floe around 01:19 UTC, which is identified in the TBs of the 22 and 31 GHz channels (Fig. 12a).

The different behavior of TBs at 243 GHz in the three cases is attributed to the interplay of $T_{\text{b,atm}}$ (which is, for example, lower on 8 August compared to 18 July), and different ice temperatures and emissivities. For example, we do not expect surface melt on 8 August (ice surface temperatures were below freezing) in contrast to 18 July, and the presence of liquid water strongly affects the dielectric permittivity and, in turn, the emissivity of the ice surface.

Brightness temperature statistics

Before analyzing the surface emissivities in more detail, we examine the statistics of all measured surface TBs during the campaign. The distribution of the surface TBs of all measurements during the cruise are shown in Figs 7 to 10 as density plots.

Fig. 7 shows the brightness temperature distribution for the TBs between 22 to 31 GHz. Here, we assume that the atmosphere does not dominate the signal. Indeed, we observe that the surface signal is evident. The prominent peaks around 160 K correspond to open water, while the peaks around 260 K correspond to observations of the ice.

At the frequencies in the 58 GHz oxygen absorption complex (Fig. 8) the absorption and downwelling TB of the atmosphere is higher than for the lower frequencies and we assume that the atmospheric contributions dominate the signal, especially closer to the center of the oxygen complex. Hence, we do not identify a distinction between ice and open ocean at these frequencies, except for 51.26 and 52.28 GHz. The relation of the oxygen absorption to the air temperature is indicated in Fig. 8b by additionally showing the distribution of measured air temperatures at 29 m height above sea level. Note that although two peaks are visible for
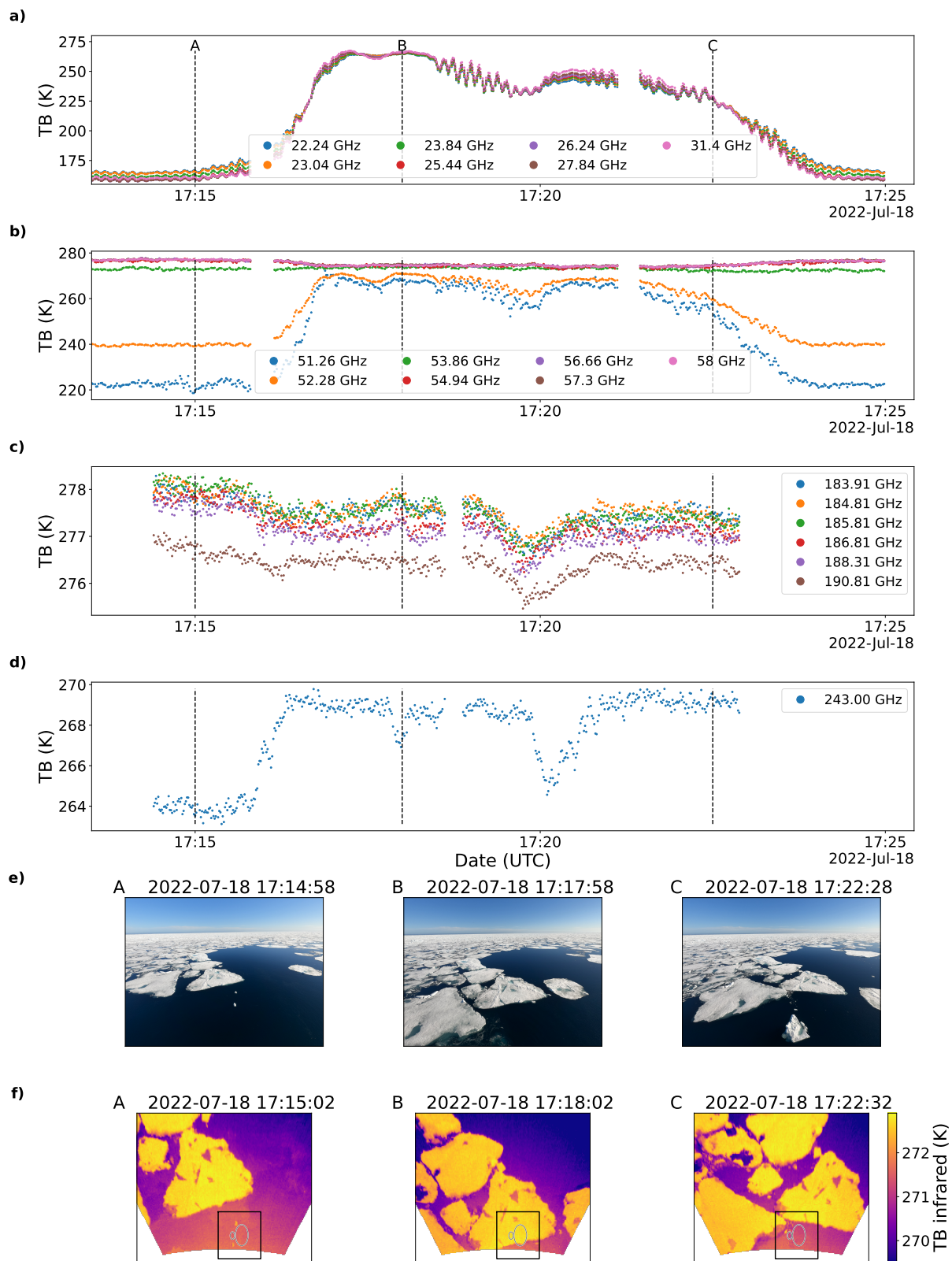
Fig. 5. HATPRO and MiRAC-P TBs on 18 July 2022 from 17:13 to 17:25 UTC for a) 22.24 to 31.4 GHz (predominantly-vertical polarization), b) 51.26 to 58 GHz (predominantly-horizontal polarization), c) 183.31 GHz (predominantly-vertical polarization) and d) 243 GHz (predominantly-horizontal polarization) measured at 53∘ zenith angle. The dashed vertical lines indicate the times of the e) visual and f) infrared camera images A, B, and C. The calculated footprints of the radiometers are indicated by the green ellipses in the IR imagery within the black rectangle.
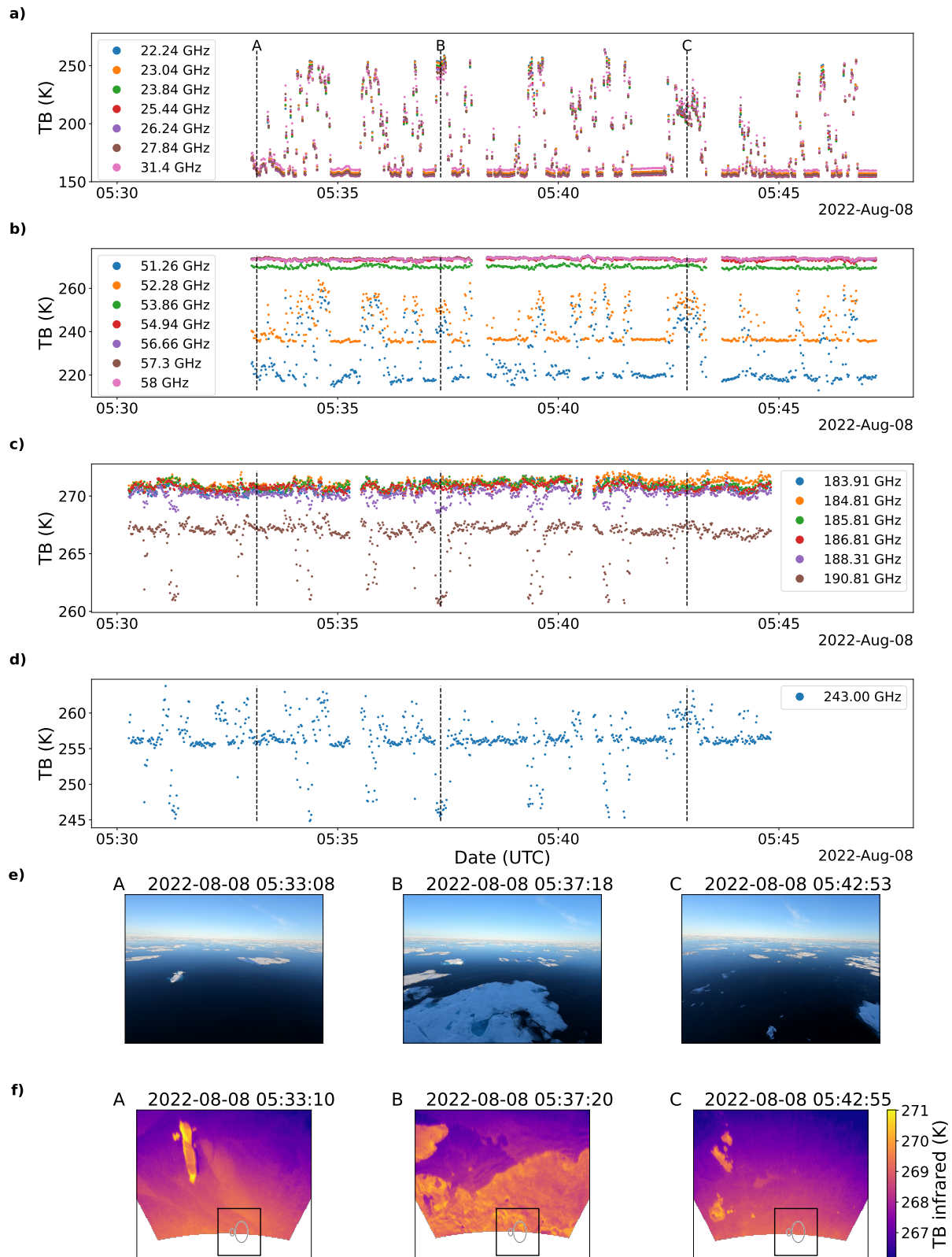
Fig. 6. Same as Fig. 5 but for 8 August 2022, 5:30 to 5:47 UTC.
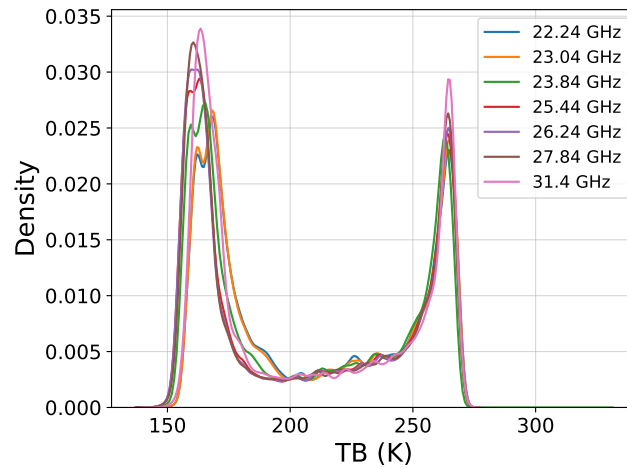
Fig. 7. All surface TB observations during ATWAICE at frequencies between 22 to 31 GHz at a 53∘ zenith angle and predominantly-vertical polarization. The total number of measurements is 500,982 (equivalent to about 139 hours). The data is shown as probability density using kernel density estimation with a Gaussian kernel.

the three highest frequencies in Fig. 8b we do not attribute them to different surface types as they do not correspond to the surface signals identified between 22 to 31 GHz.

As for the oxygen absorption complex, we assume that atmospheric contributions are dominating the observed TBs along the 183 GHz water vapor line. We observe a trimodal distribution (Fig. 9), similar to the distribution found for the IWV measurements from radiosonde data. Thus, we cannot identify a distinct surface signal.

At 243 GHz (Fig. 10), the atmospheric moisture content has a stronger influence on the TBs than at the 22 to 31 GHz channels (water vapor continuum). However, the atmosphere does not dominate the TBs as for the 183 GHz water vapor line since we do not observe a trimodal distribution here. Neither do we observe the bimodal structure as for the 22 to 31 GHz channels. At this frequency and polarization, we therefore find that ice and ocean appear to have less distinct emission signatures.

In summary, these examples show that the general idea of our measurement setup is working: the mirrors allow observations of the surface as we can identify different surface types in the measurements. We can attribute differences in the TBs at different frequencies to varying sensitivities to atmospheric parameters like water vapor. In addition, surface emissivites depending on the surface type influence the TBs and thus we continue by estimating surface emissivities.
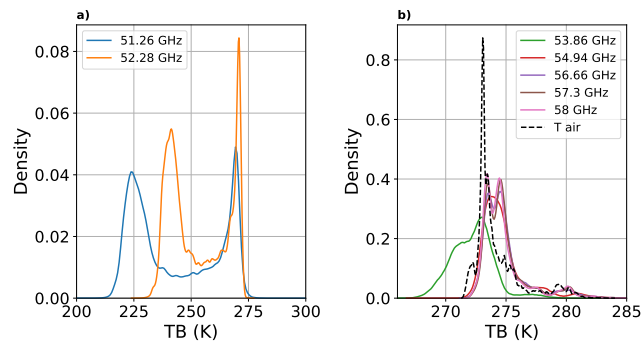
Fig. 8. All surface TB observations during ATWAICE at frequencies (a) 51.26 and 52.28 GHz and (b) between 53.86 to 58 GHz at a 53∘ zenith angle and predominantly-horizontal polarization. The total number of measurements is 485,649 (equivalent to about 135 hours). The data is shown as probability density using kernel density estimation with a Gaussian kernel. In addition the distribution of air temperatures (T air) measured onboard is shown (dashed black line).
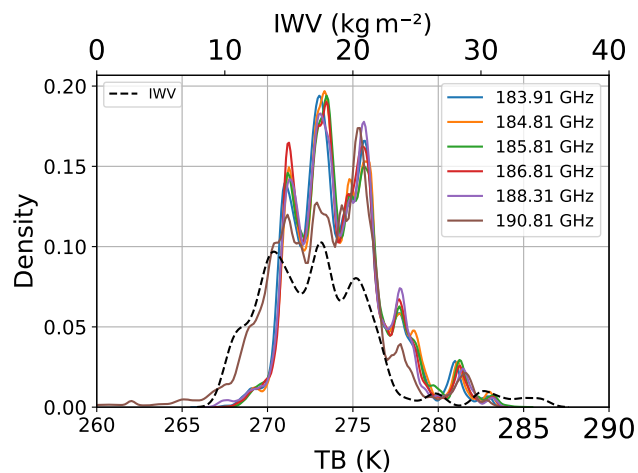

Fig. 9. All surface TB observations during ATWAICE at frequencies in the 183 GHz water vapor line at a 53∘ zenith angle and predominantly-vertical polarization. The total number of measurements is 600,607 (equivalent to about 167 hours). The data is shown as probability density using kernel density estimation with a Gaussian kernel. In addition the distribution of integrated water vapor (IWV) derived from 117 radiosonde measurements is shown (dashed black line).
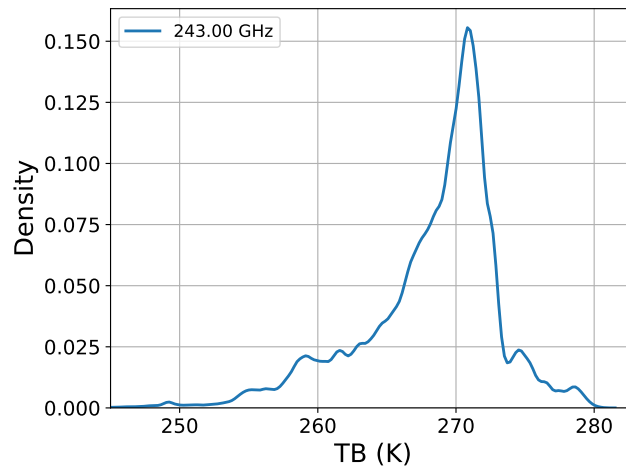
Fig. 10. Same as Fig. 7 but for 243 GHz, predominantly-horizontal polarization. The total number of measurements is 600,607 (equivalent to about 167 hours).

Surface emissivity ϵ

Due to the short atmospheric pathway (about $37\,\mathrm{m}$), we neglect atmospheric radiation and atmospheric absorption between the surface and the radiometer in our study as also done in Tucker III and others (1991) or NORSEX (1983) and use Eq. 2 to derive surface emissivities. This assumption is neither fully valid for the $183\,\mathrm{GHz}$ water vapor line and the $58\,\mathrm{GHz}$ oxygen absorption complex nor in the case of low-level fog for all frequencies. Therefore, to reduce the uncertainty in calculating ϵ, we consider clear-sky cases only in the following and constrain our estimates to the channels between 22 to $31\,\mathrm{GHz}$, 51.26, 52.28, and $243\,\mathrm{GHz}$. The selection criteria are (i) observation periods in sea ice areas and (ii) clear-sky. The first condition implies calm sea conditions, thus limiting our analysis to cases where the influence of sea surface roughness, foam and whitecaps is negligible. We distinguish clear-sky conditions by analyzing the red-blue-ratio (e.g., Long and others, 2006) captured by the sky camera and categorize pixels with a red-blue-ratio exceeding 0.7 as cloudy. In addition, we exclude conditions when atmospheric downwelling TBs are unsteady by rejecting observations if the standard deviations of the zenith observations in the 15 minutes before the surface observation are above the assumed uncertainties in $T_{\mathrm{b,atm}}$ (see next paragraph). The hereby selected times are indicated in Fig. 2. The mean air temperature during the selected periods was $2.9\,^\circ C$ (with minimum and maximum values of -1.0 and $9.2\,^\circ C$, respectively).

Estimation of $T_{\mathrm{b,atm}}$

Due to the mirror position, it was not possible to directly measure the downwelling TBs under a zenith angle of 53∘ (see Fig. 4). When we assume specular reflections, these TBs would equal $T_{\mathrm{b,atm}}$ in Eq. 1. Therefore, we estimate them using an empirical relation for the measured TBs of the radiometers viewing in zenith direction measured directly before and after the surface observations. To derive an empirical relation, we use the radiosondes launched at least twice a day (12:00 and 00:00 UTC) as model input to the Passive and Active Microwave TRAnsfer tool (PAMTRA; Mech and others, 2020) to calculate the downwelling TBs at zenith angles of $0∘$ $(T_{b,atm,0}∘)$ $and 53∘$ $(T_{\mathrm{b,atm}})$. The scatter plots and fitted linear least-squares relations are shown in Appendix Fig. 13. $T_{\mathrm{b,atm}}(t)$ at time t is then given as $T_{\mathrm{b,atm}}(t) = a_1 \cdot T_{b,atm,0}∘(t) + a_2$, with the coefficients a_1 and a_2 given by the regression (annotated in Fig. 13). $T_{b,atm,0}∘(t) is derived from linearly interpolating measured T_{b,atm,0}∘ before and after the surface observations.$

Based on the scatter plots and the measurement uncertainty of the radiometers as well as on the standard deviations of the atmospheric observations within 15 min before the surface observations (on the order of 0.15 K around 22.24 GHz and 0.6 K for 243 GHz), the overall uncertainty of $T_{\mathrm{b,atm}}$ is estimated to be 1 K for the frequencies around 22.24 GHz and 3 K for 243 GHz.

Estimation of T_{s}

Using the opening angles of the IR camera and the MWRs, we estimate a footprint position and size within the IR measurements. Note that the elliptical footprints differ depending on the frequency. We have to account for uncertainties originating from a drift in the timestamps recorded by the IR camera and uncertainties of the measured zenith angle affecting the projection of the IR imagery. The timestamp was manually corrected by comparing the IR imagery to the VIS images that provide a GPS-derived timestamp. Still, to consider these uncertainties, we use a rectangular box here (larger than the calculated elliptical footprints, shown as a black outline in Figs. 5 and 6) and estimate the uncertainty of the surface temperature using the variability of T_{s} within that rectangle. Because the cruise was conducted in the melting season, the IR temperatures of ocean, ice, and melt pond are similar. The standard deviation within our defined rectangle is usually below 1 K.

The thermal IR measured TBs averaged within the rectangular footprint are then converted to physical surface temperatures using an IR emissivity of 0.996 (Thielke, 2023). The uncertainty of the IR emissivity adds to the overall uncertainty of T_{s}, which we estimate to be 1.5 K. Every 5 s, a thermal IR image is

taken, and for the following calculation we select the coinciding TB measurements.

Estimation of emissivities and their uncertainties

The uncertainty of the derived emissivities $\Delta\epsilon$ can be estimated using a Gaussian propagation of uncertainty. The resulting expression is given by

$$\Delta\epsilon = \left|\frac{1}{T_\text{s} - T_\text{b,atm}}\right|\sqrt{(\Delta T_\text{b})^2 + A(\Delta T_\text{s})^2 + B(\Delta T_\text{b,atm})^2} \tag{5}$$

where

$$A = \frac{(T_\text{b,atm} - T_\text{b})^2}{(T_\text{s} - T_\text{b,atm})^2}$$
$$B = \frac{(T_b - T_\text{s})^2}{(T_\text{s} - T_\text{b,atm})^2}.$$

Equation 5 contains the individual uncertainties of T_s, ΔT_s, estimated to be $1.5\,\text{K}$, of $T_\text{b,atm}$, $\Delta T_\text{b,atm}$, which are 1 and $3\,\text{K}$ between 22 to $31\,\text{GHz}$ and $243\,\text{GHz}$, respectively, and the uncertainty of the radiometer TB measurements, ΔT_b, estimated to be $0.5\,\text{K}$. Note that ΔT_b would be higher when assuming a mirror that is not perfectly reflective. Also, $\Delta\epsilon$ is proportional to $(T_\text{s} - T_\text{b,atm})^{-1}$. That means $\Delta\epsilon$ is high when the downwelling $T_\text{b,atm}$ is close to the surface temperature T_s. This is of importance at $243\,\text{GHz}$, where $T_\text{b,atm}$ and T_s are of the same order of magnitude. Therefore, we exclude calculated values of ϵ with uncertainties higher than 0.025 in the following, reducing the relative uncertainties of the individual measurements to below 5%. For the remaining data, the resulting calculated average uncertainties are 0.005 between 22 to $31\,\text{GHz}$, 0.011 and 0.016 for 51.26 and $52.28\,\text{GHz}$, and 0.022 for $243\,\text{GHz}$. The difference between specular and Lambertian reflections is minimal near our observation angle (Mätzler, 2005), so our assumption about specular reflections in deriving $T_\text{b,atm}$ hardly contributes to our uncertainty estimates. To support the interpretation of the derived surface emissivities, we extracted the RGB values from the VIS camera observation closest in time and within an area containing the radiometer footprints. A statistical analysis of emissivity and RGB values provides reasonable results, despite high collocation uncertainties.

Fig. 11a shows a scatter plot and histograms with kernel density estimates of the ratio of red (R) to blue (B) from the VIS camera and the emissivities at $22.24\,\text{GHz}$. The left, low emissivity peak of ϵ corresponds to open ocean (low R to B values) and the peak at the higher emissivities to ice surfaces (high R to B value). The calculated emissivities for the other frequencies between 22 and $31\,\text{GHz}$ are shown in

Fig. 14. The maximum of the ocean emissivity shifts with increasing frequencies (from 0.51 to 0.55), while the maximum emissivity of ice lies between 0.95 and 0.96. Here, values for 23.84 GHz are slightly lower than for the other frequencies (but still within the derived uncertainty). We cannot rule out that this is a systematic uncertainty stemming from, e.g., the instrument or the liquid nitrogen calibration.

We often observe values between the two peaks that we attribute to different surface types being present within the footprint. Fig. 15 shows the derived emissivities at 51.26 and 52.28 GHz. They resemble the ones at lower frequency with an ocean emissivity around 0.57 and ice emissivities around 0.94 but with wider peaks and more intermediate emissivities occurring.

Fig. 11b shows the derived emissivities at 243 GHz. For this frequency, the distinction between different surface types is less pronounced. Here, we attribute the second peak around 0.78 to the ocean and the higher values above 0.80 to ice and mixed surface types. These higher values correspond for example to the sea ice observed on 18 July (Fig. 5) and to the young ice observed on 8 August (Fig. 6). Note that for the young, dark-looking ice we do not expect high R to B values. In addition, we can observe a small and broad peak around 0.67. These are emissivities of ice, as well observed, e.g., on 8 August (corresponding to the low TBs in Fig. 6d). The widths of the modal peaks for the different surface types can be attributed to a variety of causes. In addition to the natural variability of emissivity for different ice types and the induced uncertainties, we might observe mixed surface types (ice and open water) in the footprint, as discussed before. Furthermore, varying zenith angles (e.g., by ship movement) contribute to a high variability of ϵ over open ocean and, likely to a lesser degree, also over ice.

Table 2 summarizes the estimated emissivities by listing the maximum values of the surface modes and their widths. The values are found by fitting bi- and trimodal distributions, given as sum of normal distributions, to the data, i.e., the values are means and standard deviations of the fitted Gaussian distributions. The estimated emissivities agree with a modelling study by Willmes and others (2014) who estimate emissivities above 0.94 with a monthly standard deviation of 0.04 in June at 19 GHz, 50∘ viewing angle. Our observations also align with previously reported emissivity values, see Table 3, that show values up to 0.96 at $21\,GHz$ vertical polarization and 50∘ viewing angle. Converted to our predominantly-vertical polarization measurements this would result in an emissivity of 0.94 according to Equation 3. However, also values as low as 0.79 (0.73) for vertical (predominantly-vertical, converted by Equation 3) polarization are reported for multiyear ice in September. To our knowledge there are no estimates of emissivities at $243\,GHz$ off-nadir, thus we show literature values at nadir in Table 3 where comparisons should be ap-

Table 2. Calculated emissivities ϵ at 53∘ zenith angle for different surface types and their variability σ_ϵ, given by the width of Gaussian functions fitted to the multimodal distribution of the data

Frequency (GHz)	Polarization	ocean ϵ	ice ϵ
22.24	PV	0.507 ± 0.012	0.952 ± 0.016
23.04	PV	0.512 ± 0.012	0.953 ± 0.015
23.84	PV	0.514 ± 0.011	0.947 ± 0.016
25.44	PV	0.521 ± 0.010	0.955 ± 0.013
26.24	PV	0.525 ± 0.010	0.958 ± 0.011
27.84	PV	0.532 ± 0.010	0.958 ± 0.011
31.40	PV	0.550 ± 0.010	0.958 ± 0.011
51.26	PH	0.567 ± 0.021	0.940 ± 0.025
52.28	PH	0.576 ± 0.020	0.939 ± 0.025
243.0	PH	0.788 ± 0.010	0.661 ± 0.037 (ice 1)
			0.830 ± 0.036 (ice 2)

proached with greater caution. The values of this study for one ice type (above 0.8) fit to the literature while the lower ice emissivities of 0.67 have not been reported previously.

CONCLUSIONS AND OUTLOOK

The presented mirror construction is a low-cost addition for ship-based, upward-viewing MWRs that complements the atmospheric measurements by allowing for surface observations in the microwave spectrum along a ship track. In particular, for the TBs of the frequencies between 22 and 31 GHz, different surface types are clearly distinguishable. Such measurements are very beneficial since they can be used to describe the spatial variability of TBs and, thus, the spatial variability of surface emissivity at these frequencies for a larger area, i. e., a satellite footprint. In contrast to on-ice MWR surface measurements, the along-track observations can resolve the spatial variability of the surface conditions, including small-scale features like leads and melt ponds. Especially in summer and in the marginal ice zone, these small-scale features, which the satellite footprints cannot resolve, pose a great challenge for microwave satellite retrievals, in particular regarding the description of the surface emissivity. Therefore, our measurements help to improve the understanding of surface emissivity variability on a satellite footprint scale. Our data might help to further characterize surface contributions to the satellite signals also at 243 GHz where little in-situ data
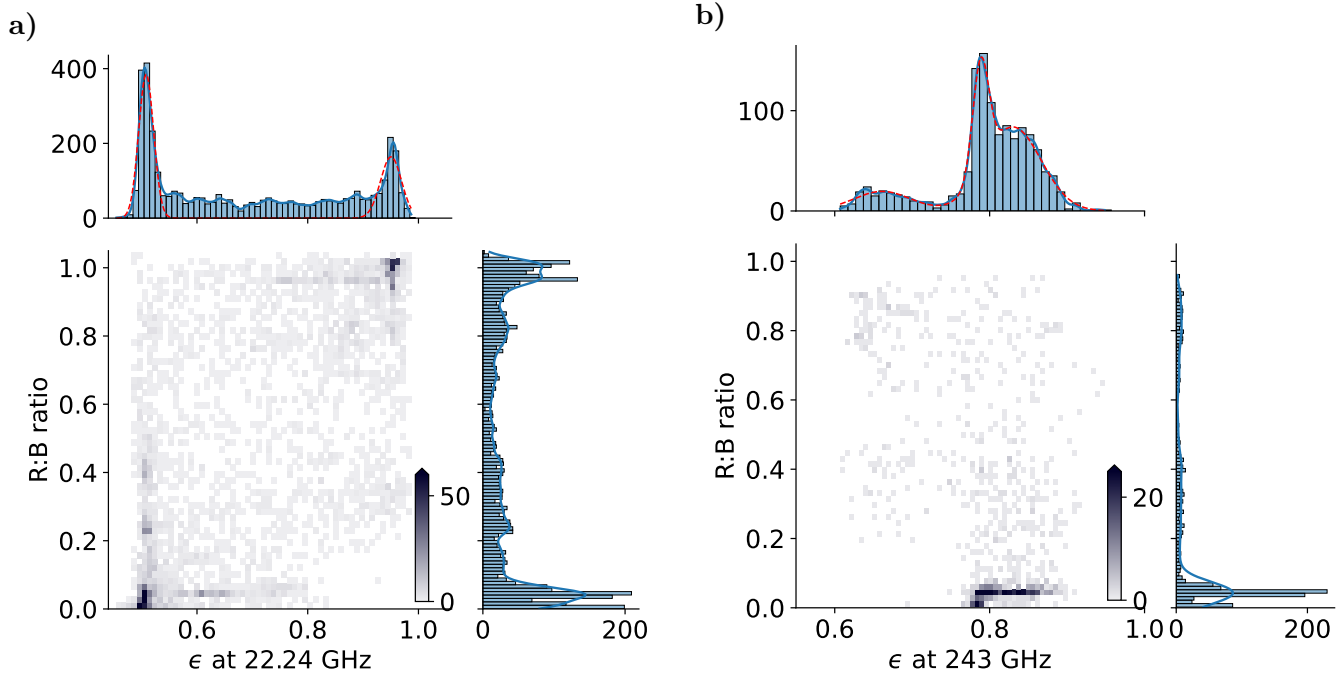
Fig. 11. Bivariate and marginal histograms with kernel density estimates (blue line) of the red (R) to blue (B) ratio of the RGB values from the visual camera and the calculated microwave emissivities ϵ in a) for 22.43 GHz (predominantly-vertical polarization) and in b) for 243 GHz (predominantly-horizontal polarization). The shown cases have been manually selected for clear-sky situations and uncertainties in ϵ smaller than 0.025, resulting in 3,730 (a) and 1,100 (b) measurements. The R to B ratio has been calculated for the MWR footprint area. The dashed red lines are Gaussian functions fitted to the data.

is currently available. This is also of interest for upcoming satellite missions like the Metop-SG Ice Cloud Imager which will use high frequencies, i. e., 183 GHz and above, for improved atmospheric sounding.

In addition, our TB data and the complementing in-situ ice observations can be used in further modeling studies. Understanding the wide range of calculated emissivities at 243 GHz over ice requires additional measurements and more detailed analysis. Here, observations at both polarizations separately would be helpful, in particular for measurements close to the Brewster angle where difference between the polarizations are potentially large.

Analyzing the zenith-angle dependence of the emitted radiation was not feasible because it was impossible to separate the angle dependence from the changing surfaces in the field of view. In the future, this is an option for ocean surfaces or cases with less spatial surface heterogeneity.

Calculating emissivities is challenged by a variety of uncertainties. Besides surface temperature uncertainties, the highest ones stem from the atmosphere. Under foggy conditions, the atmosphere between the radiometer and the ground cannot be neglected. Also, the reflected atmospheric radiation needs to be considered, which could not be directly measured. To circumvent this limitation, we estimated the $T_{\mathrm{b,atm}}$ at a zenith angle of 53○ using a regression method based on the zenith atmospheric observations of the MWRs. This estimate of $T_{\mathrm{b,atm}}$ is thus also related to some uncertainties.

Finally, we measured only one mixed polarization (predominantly-vertical or predominantly-horizontal) with each radiometer. We provide Equations 3 and 4 to calculate the polarization mixing if both horizontal and vertical polarization are known. This, however, also means that our results can only be compared to measurements from other campaigns if radiometers that measures both polarizations are used (or if exactly the same setup as ours is used).

Despite these constraints, the measurement setup allowed us to measure microwave emissions of ice and ocean surfaces and their variability on a spatial scale that resembles a satellite footprint.

For the frequency range between 22 to 31 GHz, predominantly-vertical polarization, we find that open water emissivities are between 0.508 and 0.550 (increasing with frequency). The widths of the modal peaks in the emissivity distributions serve as a measure of the variability and are between 0.010 and 0.012. Over sea ice, emissivity values range from 0.947 to 0.959 and the variabilities from 0.010 to 0.017. In this frequency range the uncertainty of ϵ is estimated to be 0.005 and thus lower than the variability derived from the distribution. At 243 GHz, predominantly-horizontal polarization, the modal peaks in the emissivity distribution are not as strictly separated as at the low frequencies. We attribute the modal peak

around around 0.783 with a variability of 0.010 to open water. The other two broader modes correspond to sea ice, with one at a lower emissivity around 0.661 and one at a higher emissivity around 0.830. The variabilities of the modes are 0.037 and 0.036.

In the future, the measurement design will be improved to quickly switch between surface and atmospheric scans under varying zenith angles. This data and observations from upcoming measurement campaigns will thus greatly help improve and develop satellite retrieval algorithms, particularly for microwave frequencies higher than $183\,\mathrm{GHz}$ that will become operational on future satellite missions.

DATA AVAILABILITY

ACKNOWLEDGEMENTS

REFERENCES

Alfred-Wegener-Institut Helmholtz-Zentrum für Polar-und Meeresforschung (2017) Polar Research and Supply Vessel POLARSTERN operated by the Alfred-Wegener-Institute. *Journal of large-scale research facilities JLSRF*, **3**, A119, ISSN 2364-091X (doi: 10.17815/jlsrf-3-163)

Crewell S and 16 others (2021) A systematic assessment of water vapor products in the Arctic: From instantaneous measurements to monthly means. *Atmospheric Measurement Techniques*, **14**(7), 4829–4856, ISSN 1867-8548 (doi: 10.5194/amt-14-4829-2021)

Ebell K, Löhnert U, Päschke E, Orlandi E, Schween JH and Crewell S (2017) A 1-D variational retrieval of tem-

perature, humidity, and liquid cloud properties: Performance under idealized and real conditions. *Journal of Geophysical Research: Atmospheres*, **122**(3), 1746–1766, ISSN 2169-897X (doi: 10.1002/2016JD025945)

Gloersen P, Nordberg W, Schmugge TJ, Wilheit TT and Campbell WJ (1973) Microwave signatures of first-year and multiyear sea ice. *Journal of Geophysical Research (1896-1977)*, **78**(18), 3564–3572 (doi: 10.1029/JC078i018p03564)

Grenfell TC and Lohanick AW (1985) Temporal variations of the microwave signatures of sea ice during the late spring and early summer near Mould Bay NWT. *Journal of Geophysical Research: Oceans*, **90**(C3), 5063–5074 (doi: 10.1029/JC090iC03p05063)

Haggerty JA and Curry JA (2001) Variability of sea ice emissivity estimated from airborne passive microwave measurements during FIRE SHEBA. *Journal of Geophysical Research: Atmospheres*, **106**(D14), 15265–15277 (doi: 10.1029/2000JD900485)

Harlow RC (2011) Sea Ice Emissivities and Effective Temperatures at MHS Frequencies: An Analysis of Airborne Microwave Data Measured During Two Arctic Campaigns. *IEEE Transactions on Geoscience and Remote Sensing*, **49**(4), 1223–1237, ISSN 1558-0644 (doi: 10.1109/TGRS.2010.2051555)

Hewison T, Selbach N, Heygster G, Taylor J and McGrath A (2002) Airborne measurements of Arctic sea ice, glacier and snow emissivity at 24-183 GHz. In *IEEE International Geoscience and Remote Sensing Symposium*, volume 5, 2851–2855, IEEE, Toronto, Ont., Canada, ISBN 978-0-7803-7536-9 (doi: 10.1109/IGARSS.2002.1026797)

Hollinger JP, Troy Jr BE, Ramseier RO, Asmus KW, Hartman MF and Luther CA (1984) Microwave emission from high Arctic sea ice during freeze-up. *Journal of Geophysical Research: Oceans*, **89**(C5), 8104–8122 (doi: 10.1029/JC089iC05p08104)

Hutchings J, Delamere J and Heil P (2020) *The Ice Watch Manual*

Kanzow T (2023) The Expedition PS131 of the Research Vessel POLARSTERN to the Fram Strait in 2022 (doi: 10.57738/BzPM_0770_2023)

Long CN, Sabburg JM, Calbó J and Pagès D (2006) Retrieving Cloud Characteristics from Ground-Based Daytime Color All-Sky Images. *Journal of Atmospheric and Oceanic Technology*, **23**(5), 633–652, ISSN 1520-0426, 0739-0572 (doi: 10.1175/JTECH1875.1)

Mätzler C (2005) On the Determination of Surface Emissivity From Satellite Observations. *IEEE Geoscience and Remote Sensing Letters*, **2**(2), 160–163, ISSN 1545-598X (doi: 10.1109/LGRS.2004.842448)

Mätzler C, Ramseier R and Svendsen E (1984) Polarization effects in seaice signatures. *IEEE Journal of Oceanic Engineering*, **9**(5), 333–338, ISSN 0364-9059 (doi: 10.1109/JOE.1984.1145646)

Mech M, Kliesch LL, Anhäuser A, Rose T, Kollias P and Crewell S (2019) Microwave Radar/radiometer for Arctic Clouds (MiRAC): First insights from the ACLOUD campaign. *Atmospheric Measurement Techniques*, **12**(9), 5019–5037, ISSN 1867-8548 (doi: 10.5194/amt-12-5019-2019)

Mech M and 7 others (2020) PAMTRA 1.0: The Passive and Active Microwave radiative TRAnsfer tool for simulating radiometer and radar measurements of the cloudy atmosphere. *Geoscientific Model Development*, **13**(9), 4229–4251, ISSN 1991-9603 (doi: 10.5194/gmd-13-4229-2020)

NORSEX G (1983) Norwegian Remote Sensing Experiment in a Marginal Ice Zone. *Science*, **220**(4599), 781–787 (doi: 10.1126/science.220.4599.781)

Onstott RG, Grenfell TC, Mätzler C, Luther CA and Svendsen EA (1987) Evolution of microwave sea ice signatures during early summer and midsummer in the marginal ice zone. *Journal of Geophysical Research*, **92**(C7), 6825, ISSN 0148-0227 (doi: 10.1029/JC092iC07p06825)

Rantanen M and 7 others (2022) The Arctic has warmed nearly four times faster than the globe since 1979. *Communications Earth & Environment*, **3**(1), 168, ISSN 2662-4435 (doi: 10.1038/s43247-022-00498-3)

Risse N, Mech M, Prigent C, Spreen G and Crewell S (2024) Assessing the sea ice microwave emissivity up to submillimeter waves from airborne and satellite observations. *EGUsphere*, **2024**, 1–35 (doi: 10.5194/egusphere-2024-179)

Rose T, Crewell S, Löhnert U and Simmer C (2005) A network suitable microwave radiometer for operational monitoring of the cloudy atmosphere. *Atmospheric Research*, **75**(3), 183–200, ISSN 01698095 (doi: 10.1016/j.atmosres.2004.12.005)

Rückert JE, Walbröl A, Niehaus H and Spreen G (2023a) Sea ice density and salinity profiles measured during RV POLARSTERN cruise PS131 [dataset]. PANGAEA. (doi: 10.1594/PANGAEA.961670)

Rückert JE, Walbröl A and Spreen G (2023b) Sea ice temperature profiles measured during RV POLARSTERN cruise PS131 [dataset] PANGAEA (doi: 10.1594/PANGAEA.961656)

Rückert JE, Niehaus H, Walbröl A and Spreen G (2024a) Visual images of the surface taken by a camera installed on RV POLARSTERN during expedition PS131 (ATWAICE) (June - august A022, Fram Strait/East Greenland) [dataset] PANGAEA (doi: 10.1594/PANGAEA.967580)

Rückert JE, Spreen G, Huntemann M, Niehaus H and Walbröl A (2024b) Surface brightness temperature images measured by an infrared camera installed on RV POLARSTERN during expedition PS131 (ATWAICE) (June - August 2022, Fram Strait/East Greenland) [dataset] PANGAEA (doi: 10.1594/PANGAEA.967576)

Rückert JE, Walbröl A, Spreen G, Ebell K and Mech M (2024c) Surface brightness temperatures measured by the HATPRO microwave radiometer onboard the RV Polarstern during the ATWAICE expedition PS144 to the Arctic in summer 2022 [dataset] (doi: 10.5281/ZENODO.11396941)

Rückert JE, Walbröl A, Spreen G, Ebell K and Mech M (2024d) Surface brightness temperatures measured by the MiRAC-P microwave radiometer onboard the RV Polarstern during the ATWAICE expedition PS144 to the Arctic in summer 2022 [dataset].(doi: 10.5281/ZENODO.11396749)

Spreen G, Kaleschke L and Heygster G (2008) Sea ice remote sensing using AMSR-E 89-GHz channels. *Journal of Geophysical Research*, **113**(C2), C02S03, ISSN 0148-0227 (doi: 10.1029/2005JC003384)

Thielke L (2023) *Winter Sea Ice Characteristics in the Central Arctic from Thermal Infrared Imaging*. Ph.D. thesis, University of Bremen (doi: 10.26092/elib/2305)

Tucker III WB and 6 others (1991) Microwave and physical properties of sea ice in the winter Marginal Ice Zone. *Journal of Geophysical Research: Oceans*, **96**(C3), 4573–4587 (doi: 10.1029/90JC02269)

Wendisch M and 136 others (2023) Atmospheric and Surface Processes, and Feedback Mechanisms Determining Arctic Amplification: A Review of First Results and Prospects of the (AC)3 Project. *Bulletin of the American Meteorological Society*, **104**(1), E208–E242, ISSN 0003-0007, 1520-0477 (doi: 10.1175/BAMS-D-21-0218.1)

Westwater ER (1978) The accuracy of water vapor and cloud liquid determination by dual-frequency ground-based microwave radiometry. *Radio Science*, **13**(4), 677–685, ISSN 0048-6604, 1944-799X (doi: 10.1029/RS013i004p00677)

Wilheit T, Nordberg W, Blinn J, Campbell W and Edgerton A (1971) Aircraft measurements of microwave emission from Arctic Sea ice. *Remote Sensing of Environment*, **2**, 129–139, ISSN 0034-4257 (doi: 10.1016/0034-4257(71)90087-3)

Willmes S, Nicolaus M and Haas C (2014) The microwave emissivity variability of snow covered first-year sea ice from late winter to early summer: A model study. *The Cryosphere*, **8**(3), 891–904, ISSN 1994-0424 (doi: 10.5194/tc-8-891-2014)

APPENDIX

Fig. 12 shows the TB measurements around 80○57.38′N, 8○41.01′E on 19 July 19 2022, 01:13 to 01:22 UTC when the vessel was traveling with a mean speed of 0.2 ms. Atmospheric HATPRO measurements right before and after yield IWV values of 17.5 to 17.7 kg m^{-2}. The averaged air temperature during the observation period is 2.9 ○C. The bright spots in IR imagery are seabirds.

Fig. 13 shows the simulations used to derive TBs under a zenith angle of 53○. Shown are the TBs simulated from 124 radiosoundings using the PAMTRA tool as scatterplots for the frequencies between 22 and 31 GHz and 243 GHz. The red lines are fitted linear least-squares regressions.

Fig. 14 is a density plot of ϵ calculated for the frequencies between 22 and 31 GHz as described in the main text.

Table 3 lists measurements of emissivities for the channels we used but we would like to mention that Harlow (2011) and Hewison and others (2002) also report emissivity calculations at frequencies around 183 GHz, the latter also 50 GHz, but only for nadir observations.
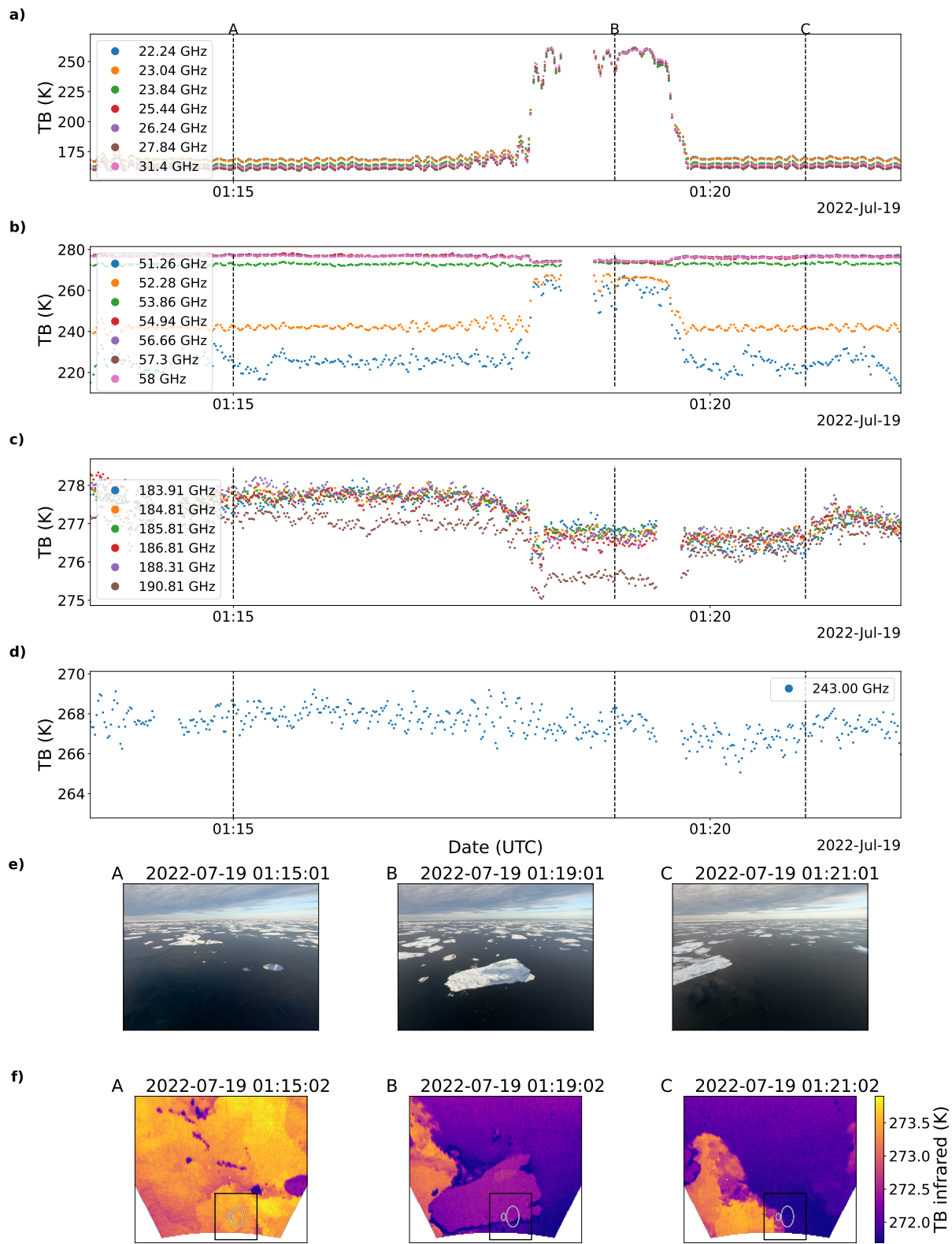
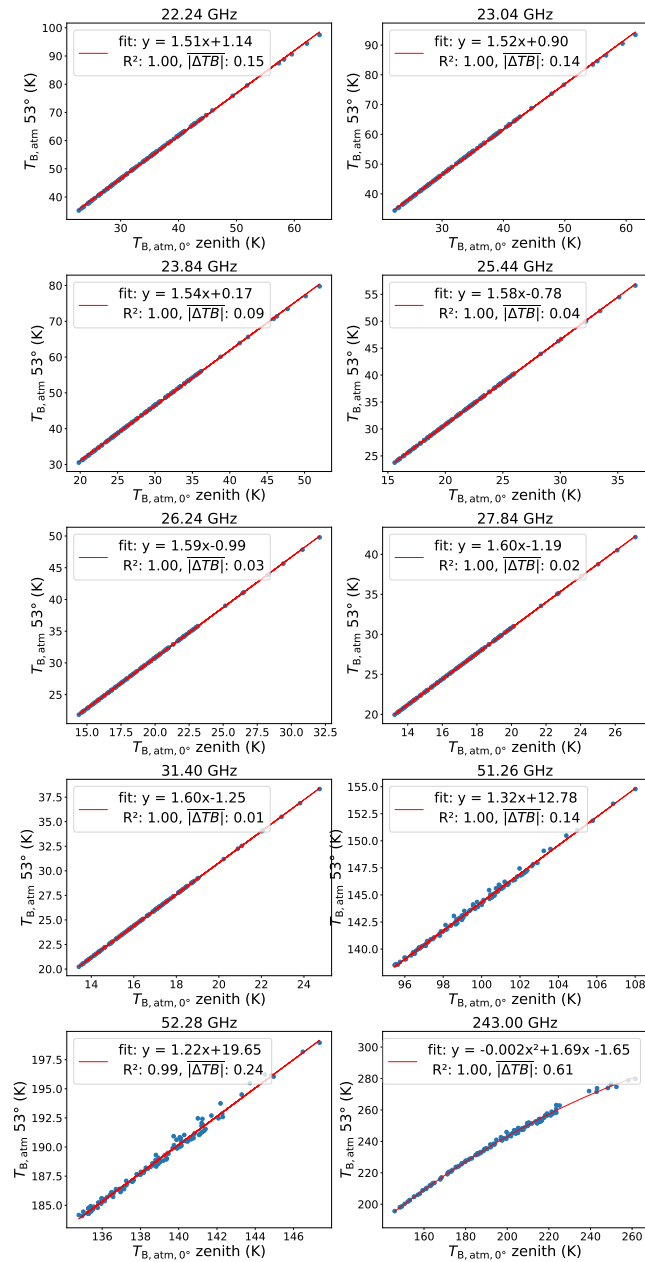**Fig. 12.** Same as Fig. 5 but for 19 July 2022, 01:13 to 01:22 UTC.

Fig. 13. Scatterplots of simulated TBs of different frequencies under a zenith angle of 53∘ and of 0∘. Input to the simulations with PAMTRA are the radiosonde data from the ATWAICE campaign. The number of simulations is 124. Annotated in the plots are the coefficients from a linear least-squares regression (quadratic fit for 243 GHz) and the mean absolute difference between the data and predicted values.
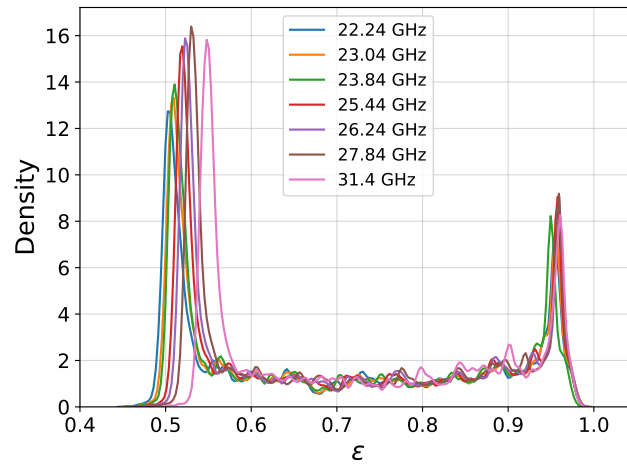
Fig. 14. Kernel density estimate of the distribution of emissivities (ϵ) calculated for the frequencies between 22 and 31 GHz at a 53° zenith angle for manually selected times with clear sky (N=3730).
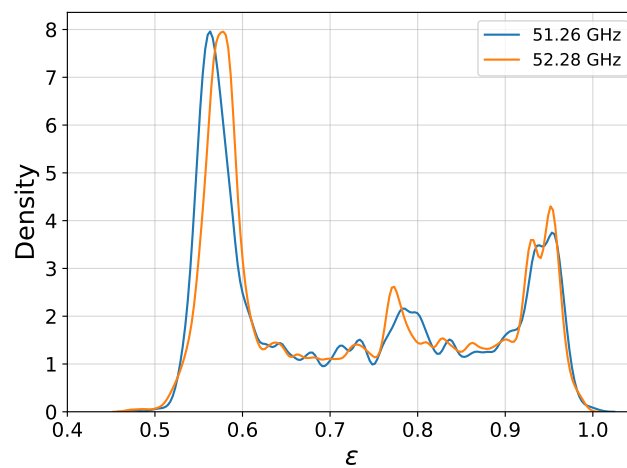

Fig. 15. Kernel density estimate of the distribution of emissivities (ϵ) calculated for the frequencies 51.26 and 52.28 GHz at a 53° zenith angle for manually selected times with clear sky (N=3730).

Table 3. Measured emissivities ϵ from previous measurement campaigns sorted by frequency. Polarization is either horizontal (H) or vertical (V). First-year ice and multiyear ice are abbreviated as FYI and MYI, respectively.

Reference	Campaign/Time	Frequency (GHz) & Polarization	Angle	ϵ
NORSEX (1983)	ship, Sept./Oct.	21 H	50	0.906±0.025/0.635±0.125 (FYI/MYI)
		21 V	50	0.953±0.003/0.787±0.08 (FYI/MYI)
Mätzler and others (1984)	ship, Sept.	21 H	50	0.78/0.80 & 0.86 (MYI/wet ice)[a]
		21 V	50	0.86/0.90 & 0.93 (multiyear/wet ice)*
Onstott and others (1987)	ship, July	21 H	50	0.90 (midsummer)/0.91 (late summer)[b]
		21 V	50	0.96[†]
Hewison and others (2002)	airborne, March	50	0	0.97/0.95±0.02/0.83±0.10 (nilas/FYI/MYI) [c]
Haggerty and Curry (2001)	airborne, May	220	0	0.84[d]
Risse and others (2024)	airborne, May/June	243	0	0.77±0.05
Risse and others (2024)	airborne, Mar./April	243	0	0.77±0.06

[a]values estimated from Fig. 4 and 7 within
[b]values estimated from Fig. 7 within
[c]values estimated from Fig. 1 within
[d]mean value, Fig. 6 within suggests a range of 0.80 to 0.86